European Journal of Radiology 134 (2021) 109467

Contents lists available at ScienceDirect

European Journal of Radiology

journal homepage: www.elsevier.com/locate/ejrad

Research article

Distinguishing brain inflammation from grade II glioma in population without contrast enhancement: a radiomics analysis based on conventional MRI

Yu Han [a,1], Yang Yang [a,1], Zhe-sheng Shi [b], An-ding Zhang [b], Lin-feng Yan [a], Yu-chuan Hu [a], Lan-lan Feng [c], Jiao Ma [c], Wen Wang [a,*], Guang-bin Cui [a,*]

[a] Department of Radiology & Functional and Molecular Imaging Key Lab of Shaanxi Province, Tangdu Hospital, Fourth Military Medical University, Xi'an, Shaanxi, 710038, PR China
[b] College of Basic Medicine, Fourth Military Medical University, Xi'an, Shaanxi, 710032, PR China
[c] Department of Pathology, Tangdu Hospital, Fourth Military Medical University, Xi'an, 710038, PR China

ARTICLE INFO

Keywords:
Radiomics
Inflammation
Glioma
Magnetic resonance imaging (MRI)

ABSTRACT

Purpose: In populations without contrast enhancement, the imaging features of atypical brain parenchyma inflammations can mimic those of grade II gliomas. The aim of this study was to assess the value of the conventional MR-based radiomics signature in differentiating brain inflammation from grade II glioma.

Methods: Fifty-seven patients (39 patients with grade II glioma and 18 patients with inflammation) were divided into primary (n = 44) and validation cohorts (n = 13). Radiomics features were extracted from T_1-weighted images (T_1WI) and T_2-weighted images (T_2WI). Two-sample *t*-test and least absolute shrinkage and selection operator (LASSO) regression were adopted to select features and build radiomics signature models for discriminating inflammation from glioma. The predictive performance of the models was evaluated via area under the receiver operating characteristic curve (AUC) and compared with the radiologists' assessments.

Results: Based on the primary cohort, we developed T_1WI, T_2WI and combination (T_1WI + T_2WI) models for differentiating inflammation from glioma with 4, 8, and 5 radiomics features, respectively. Among these models, T_2WI and combination models achieved better diagnostic efficacy, with AUC of 0.980, 0.988 in primary cohort and that of 0.950, 0.925 in validation cohort, respectively. The AUCs of radiologist 1's and 2's assessments were 0.661 and 0.722, respectively.

Conclusion: The signature based on radiomics features helps to differentiate inflammation from grade II glioma and improved performance compared with experienced radiologists, which could potentially be useful in clinical practice.

1. Introduction

World Health Organization (WHO) grade II glioma is the common primary brain tumor and surgery is the first-line treatment [1]. Brain parenchyma inflammation is a common non-tumor lesion with associated neurologic dysfunction, and non-operative therapy is the main treatment [2]. In clinical practice, clinicians should be vigilant for distinguishing inflammation from grade II glioma. In particular, in some cases, laboratory tests are atypical and clinical symptoms and signs of these entities often overlap [3–8]. This diagnostic dilemma might lead to a biopsy, an inadvertent operation, and even radiation therapy, which eventually can aggravate patient's condition. Therefore, it is of utmost importance to seek alternative noninvasive diagnostic tool to guide appropriate treatment.

Magnetic resonance imaging (MRI), as a non-radiation and non-invasive imaging technique, offers superb resolution for qualitative diagnosis of intracranial lesions [9,10]. However, MR diagnostic dilemma still exists in atypical cases for distinguishing inflammation from grade II glioma. Based on conventional MR sequences, both inflammation and glioma can manifest as lesions with mass effect,

* Corresponding authors at: Department of Radiology & Functional and Molecular Imaging Key Lab of Shaanxi Province, Tangdu Hospital, Fourth Military Medical University, 569 Xinsi Road, Xi'an, 710038, Shaanxi, PR China.
E-mail addresses: 40204024@qq.com, wangwen@fmmu.edu.cn (W. Wang), cgbtd@126.com (G.-b. Cui).
[1] Yu Han and Yang Yang contributed equally to this work.

https://doi.org/10.1016/j.ejrad.2020.109467
Received 1 October 2020; Received in revised form 22 November 2020; Accepted 1 December 2020
Available online 3 December 2020

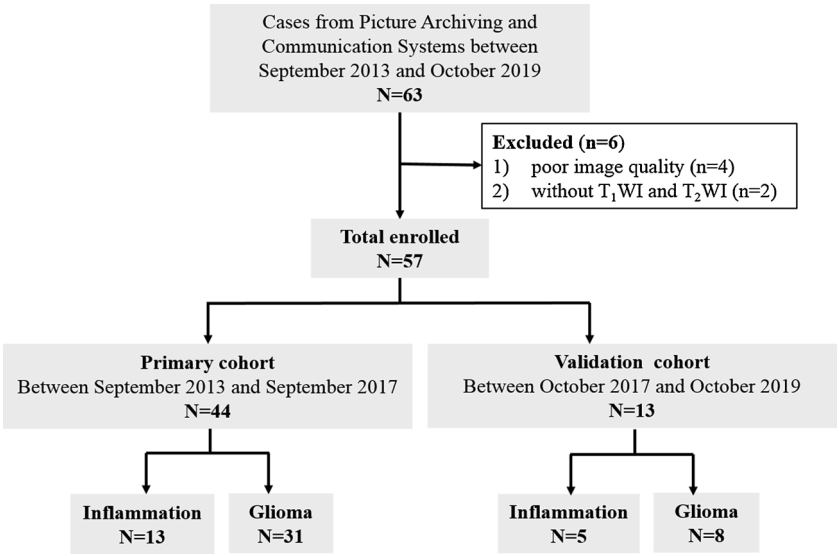

Fig. 1. Flow diagram for patient selection.

hypointensity on T_1-weighted image (T_1WI), hyperintensity on T_2-weighted image (T_2WI), no enhancement on post-contrast T_1WI (T_1CE). Although a few study reported that MRI features based on conventional MRI can help distinguish inflammatory lesions from glioma [11], but the subjective feature evaluation and lack of quantitative indicators limit its clinical application. Even though various functional MR techniques are used for differential diagnosis, no expert consensus has been established [3,12–14]. Therefore, it is urgent to find a more efficient and stable way to distinguish inflammation from glioma based on MRI in non-contrast enhanced populations.

Radiomics, which is a promising and rapidly growing discipline, refers to extraction of large number of quantitative features from medical images and converting the information into mineable data [15]. Subsequent quantitative analysis of these data can support clinical decision-making [16]. Compared with human eyes, radiomics conquer the limitation of visual assessment of images that offer little information on heterogeneity of lesions [17]. Currently, radiomics has been widely used in neurological diseases to facilitate improved clinical decision-making [18–20].

To our knowledge, there is no radiomics-based study for differentiating brain inflammation from grade II glioma in non-contrast enhanced populations. The aim of this study was to explore the utility of extracted radiomics features in discriminating brain inflammation from grade II glioma.

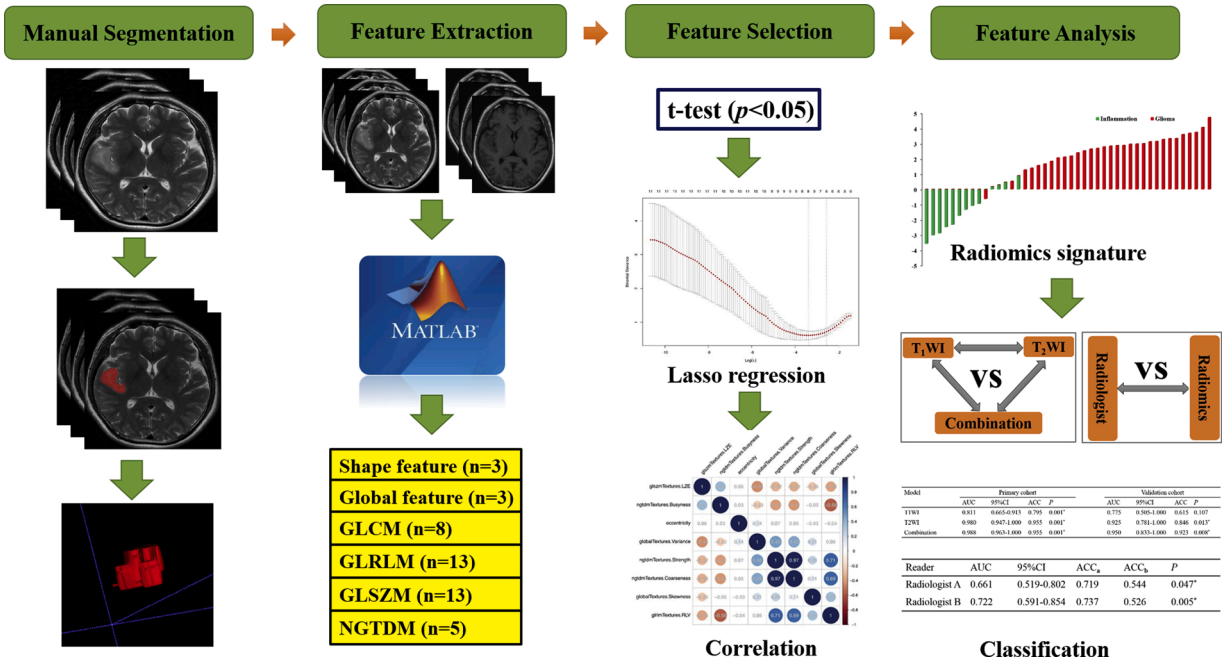

Fig. 2. Study flow chart: First, VOI segmentation was done. Second, six types of texture features within VOIs were extracted by using MATLAB 2014b (MathWorks, USA), including the shape, global, GLCM, GLRLM, GLSZM and NGTDM features. Third, two-sample *t*-test and LASSO were adopted to select features. Finally, different radiomics signature models for discriminating inflammation from glioma were constructed. The predictive performance of model was evaluated via receiver operating curve and compared with the assessment of radiologists.

Table 1
Characteristics of patients in the primary and validation cohorts.

Characteristic	Primary cohort (n = 44)			Validation cohort (n = 13)		
	Inflammation	Glioma	*P*	Inflammation	Glioma	*P*
No. of patients	13	31	NA	5	8	NA
Age			0.724			0.449
Mean ± SD	40.4 ± 14.3	42.1 ± 14.7		51.4 ± 12.4	43 ± 21.2	
Gender, n (%)			0.448			0.592
Male	10/13 (76.9)	19/31 (61.3)		3/5 (60.0)	3/8 (37.5)	
Female	3/13 (23.1)	12/31 (38.7)		2/5 (40.0)	5/8 (62.5)	
Symptom, n (%)			0.522			0.346
Seizure	4/13 (30.8)	8/31 (25.8)		2/5 (40)	1/8 (12.5)	
Headache/nausea/dizziness	3/13 (23.1)	11/31 (35.5)		1/5 (20)	3/8 (37.5)	
Loss of consciousness	0/13 (0)	3/31 (9.7)		0/5 (0)	0/8 (0)	
Dysphasia	1/13 (7.7)	2/31 (6.5)		0/5 (0)	2/8 (25)	
Blurred vison	0/13 (0)	1/31 (3.2)		0/5 (0)	0/8 (0)	
Memory deficits	2/13 (15.4)	1/31 (3.2)		1/5 (20)	0/8 (0)	
Psychiatric symptoms	1/13 (7.7)	0/31 (0)		1/5 (20)	0/8 (0)	
Numbness/weakness of limbs	2/13 (15.4)	5/31 (16.1)		0/5 (0)	2/8 (25)	
Onset, n (%)			0.205			0.239
Acute (< 2 weeks)	7/13 (53.8)	8/31 (25.8)		3/5 (60.0)	2/8 (25.0)	
Subacute (2 weeks - 3 months)	3/13 (23.1)	9/31 (29.0)		2/5 (40.0)	2/8 (25.0)	
Chronic (> 3 months)	3/13 (23.1)	14/31 (45.2)		0/5 (0)	4/8 (50.0)	
Side, n (%)			0.879			0.739
Left	8/13 (61.5)	17/31 (54.8)		4/5 (80.0)	4/8 (50.0)	
Right	4/13 (30.8)	12/31 (38.7)		1/5 (20.0)	3/8 (37.5)	
Bilateral	1/13 (7.7)	2/31 (6.5)		0/5 (0)	1/8 (12.5)	
≥2 lobe involved, n (%)			0.105			1.000
Yes	3/13 (23.1)	16/31 (51.6)		2/5 (40.0)	3/8 (37.5)	
No	10/13 (76.9)	15/31 (48.4)		3/5 (60.0)	5/8 (62.5)	
Pathologic procedure, n (%)			NA			NA
Biopsy	1/13 (7.7)	5/31 (16.1)		0	1/8 (12.5)	
Resection	12/13 (92.3)	26/31 (83.9)		5/5 (100)	7/8 (87.5)	

P values were calculated by two-sample *t*-test for continuous variables and Fisher's exact test for categorical variables.

Table 2
Radiomics features selected by two-sample *t*-test.

T_1WI (n = 19)	T_2WI (n = 26)
eccentricity; volume; glcm Textures. Contrast; glcm Textures. Homogeneity; glcm Textures. Dissimilarity; glrlm Textures. SRE; glrlm Textures. LRE; glrlm Textures. RLN; glrlm Textures. RP; glrlm Textures. RLV; glszm Textures. SZE; glszm Textures. LZE; glszm Textures. ZSN; glszm Textures. ZP; glszm Textures. ZSV; glszm Textures. LZHGE; ngtdm Textures. Coarseness; ngtdm Textures. Busyness; ngtdm Textures. Strength	eccentricity; volume; global Textures. Variance; global Textures. Skewness; glcm Textures. Entropy; glcm Textures. Homogeneity; glcm Textures. Variance; glrlm Textures. SRE; glrlm Textures. LRE; glrlm Textures. RLN; glrlm Textures. RP; glrlm Textures. LGRE; glrlm Textures. SRLGE; glrlm Textures. LRLGE; glrlm Textures. RLV; glszm Textures. LZE; glszm Textures. GLN; glszm Textures. ZP; glszm Textures. LGZE; glszm Textures. SZLGE; glszm Textures. LZHGE; glszm Textures. ZSV; ngtdm Textures. Coarseness; ngtdm Textures. Contrast; ngtdm Textures. Busyness; ngtdm Textures. Strength

2. Materials and methods

2.1. Patient population

This retrospective study was approved by local ethics committee of our hospital, and informed consent was waived. Atypical cases in our study are defined as: patients have no symptoms of prodromal infection, and no inflammatory changes in the serum and cerebrospinal fluid (CSF) tests. The antibodies related to demyelinating diseases of the central nervous system and anti-neuronal autoantibodies are also negative. On MR images, the lesion shows hypointensity on T_1WI, hyperintensity on T_2WI without obvious mass effect, no enhancement on T_1CE.

Between September 2013 and October 2019, 63 cases from the Picture Archiving and Communication Systems (PACS) were investigated consecutively. The inclusion criteria were: (1) cases where the radiology report was undecided between inflammation versus glioma (the keywords (inflammation or glioma) were set by the retrieval function of PACS); (2) inflammation or grade II glioma confirmed by pathology; (3) no history of surgery or treatment before MRI examination; (4) no enhancement on T_1CE. The exclusion criteria were as follows: (1) poor image quality such as significant motion or susceptibility artifacts; (2) incomplete imaging data.

Two cases without T_1WI and T_2WI, 4 cases with poor image quality (motion artifact, 3 cases; metal artifact, 1 case) were excluded. The final study population contained 57 cases. The included cases were then divided into two groups according to the time points. The first group (recruited from September 2013 to September 2017) consisted of 44 patients (13 inflammations and 31 gliomas). They formed the primary cohort of 29 males and 15 females (mean age, 41.6 ± 14.5 years; age range, 8–68 years). The second group (recruited from October 2017 to October 2019) consisted of 13 consecutive patients (5 inflammations and 8 gliomas). They constituted the independent validation cohort of 6 males and 7 females (mean age, 46.3 ± 17.1 years; age range, 18–72 years). The patient selection flow chart is shown in Fig. 1.

2.2. Imaging data acquisition

The whole brain MRI examinations were performed on a 3 T MRI system (Discovery MR750, General Electric Medical System, Milwaukee, WI, USA) with an eight-channel head coil (GE Medical System). Pre-contrast axial T_1WI, T_2WI and sagittal T_2WI were acquired in all cases. The imaging parameters are as follows: 1) axial T_1WI: repetition time/echo time (TR/TE), 1750 ms/24 ms; matrix size, 256 × 256; field of view (FOV), 24 × 24 cm^2; number of excitation, 1; slice thickness, 5 mm; gap, 1.5 mm. 2) T_2WI: TR/TE, 4247 ms/93 ms; matrix size, 512 × 512; FOV, 24 × 24 cm^2; number of excitation, 1; slice thickness, 5 mm; gap, 1.5 mm. 3) sagittal T_2WI: TR/TE, 4338 ms/96 ms; matrix size, 384 × 384; FOV, 24 × 24 cm^2; number of excitation, 2; slice thickness, 5 mm; gap, 1.0 mm.

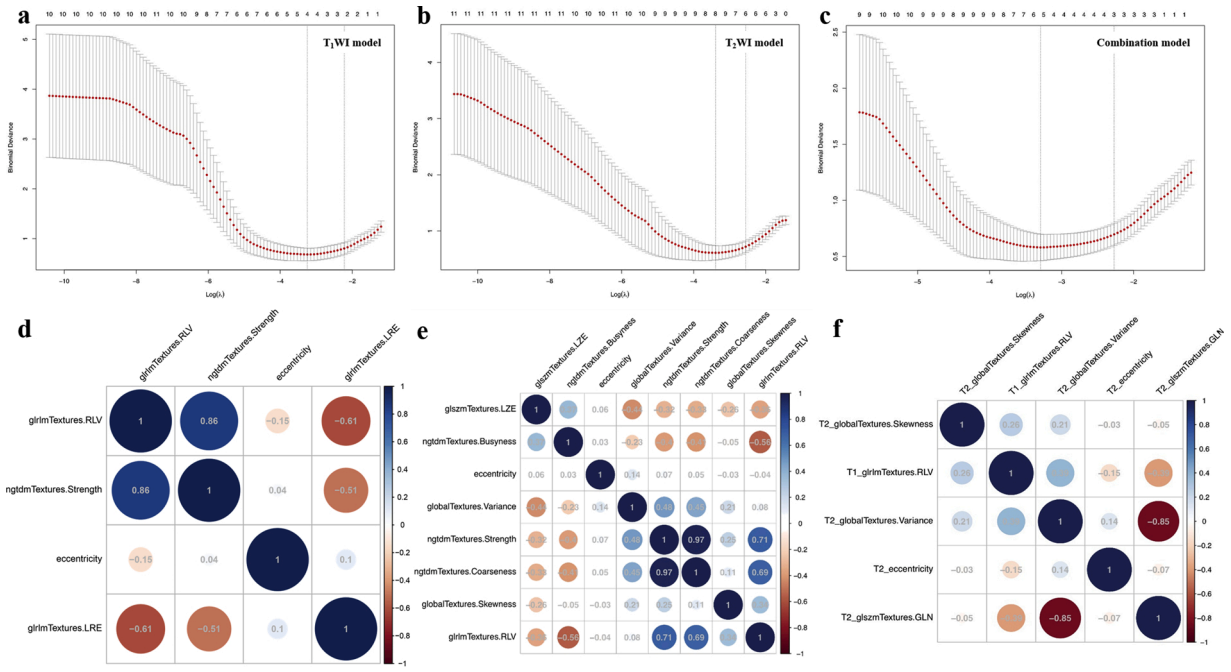

Fig. 3. Selection of features to subject LASSO regression and correlation-matrix heat map: a-c, selection of the tuning parameter (λ) in the LASSO model via 10-fold cross validation based on minimum criteria. Binomial deviances from the LASSO regression cross-validation procedure were plotted as a function of log(λ). The y-axis indicates binomial deviances. The lower x-axis indicates the log(λ). Numbers along the upper x-axis represent the average number of predictors. Red dots indicate average deviance values for each model with a given λ, and vertical bars through the red dots show the upper and lower values of the deviances. The vertical black lines define the optimal values of λ, where the model provides its best fit to the data. d-f, the correlation-matrix heat map based on the correlation between each feature pair of the selected feature.

Finally, T_1CE was acquired after intravenous administration of 0.1 mmol/kg gadopentetate dimeglumine.

2.3. Volume-of-interest segmentation and feature extraction

All images were anonymised and stored in DICOM format. Three-dimensional volume of interest (VOI) was achieved by using a free open-source software package (ITK-SNAP, version 3.6.0; http://itk-snap.org). Two experienced neuroradiologists (L.f.Y. and Y.H. who have 12 and 9 years of experience, respectively, in neuro-oncology imaging) manually outlined the edge of the entire high signal lesion area layer by layer on axial T_2WI images. For each layer, the contour line was carefully drawn while attempting to maintain an approximate distance of 2−3 mm from the lesion margin to minimize the partial volume effect. All layers were fused into a VOI (Fig. 2). Finally, VOIs on T_2WI were copied to T_1WI.

Before feature extraction, all image data were normalized by transforming the data into standardized intensity ranges for each imaging modality across all subjects, with a mean of 0 and a SD of 1 (i.e., z-score transformation). After data normalization, 3D quantitative feature extraction was conducted using MATLAB 2014b (MathWorks, USA). Three shape feature, 3 global feature, 8 gray level co-occurrence matrix (GLCM), 13 gray level run length matrix (GLRLM), 13 gray level size zone matrix (GLSZM) and 5 neighbourhood gray-tone difference matrix (NGTDM) were extracted from T_1WI and T_2WI, respectively. Therefore, for each mode, a total of 45 quantitative features were obtained. Details of the definitions and calculations of these quantitative features extracted in this study have previously been given [21–23]. To ensure intra- and inter-observer reproducibility, the robustness of all the features based on VOIs was evaluated by both test-retest and inter-rater analysis [24].

2.4. Features selection, radiomics signature building and validation

To improve the accuracy and efficiency of classification, irrelevant and redundant features were identified and excluded. Two feature selection methods were employed sequentially to select informative radiomics features from 45 features (Fig. 2). First, two sample *t*-test was adopted to select those features with statistically significant difference between inflammation and glioma ($P < 0.05$). To increase the model interpretability and reduce overfitting, least absolute shrinkage and selection operator (LASSO) regression algorithm [25] was then applied in T_1WI, T_2WI and combination model (T_1WI + T_2WI) to select a subset of the most significant radiomics features with nonzero coefficients. Radiomics signature score (Rad-score) was calculated using a linear combination of selected features weighted by the corresponding LASSO coefficients. The receiver operating characteristics (ROC) curve (AUC) was used to evaluate the predictive performance of the radiomics signature in differentiating inflammation from glioma in both the primary and validation cohort.

2.5. Pathologic diagnosis

The final diagnosis was determined by surgical or puncture biopsy specimen and confirmed with pathology. Two neuropathologists (L.l.F. and J.M., with 10 and 8 years of experience in pathological diagnosis of central nervous system diseases, respectively), who was blinded to the MR findings, re-evaluated the pathological data. Histologically, variable chronic inflammatory cell infiltration and reactive gliosis are found in the inflammatory group. In some cases, distinction between gliomas and reactive gliosis is difficult by histology alone, especially in small biopsies from the infiltrating edge of lesion. Reactive gliosis features uniformly distributed astrocytes with regular spacing within the tissue and abundant processes, which can be demonstrated by glial fibrillary acidic protein (GFAP) immunohistochemistry. In contrast, diffuse infiltrating gliomas will be less uniformly distributed, tend to form cell clusters, and

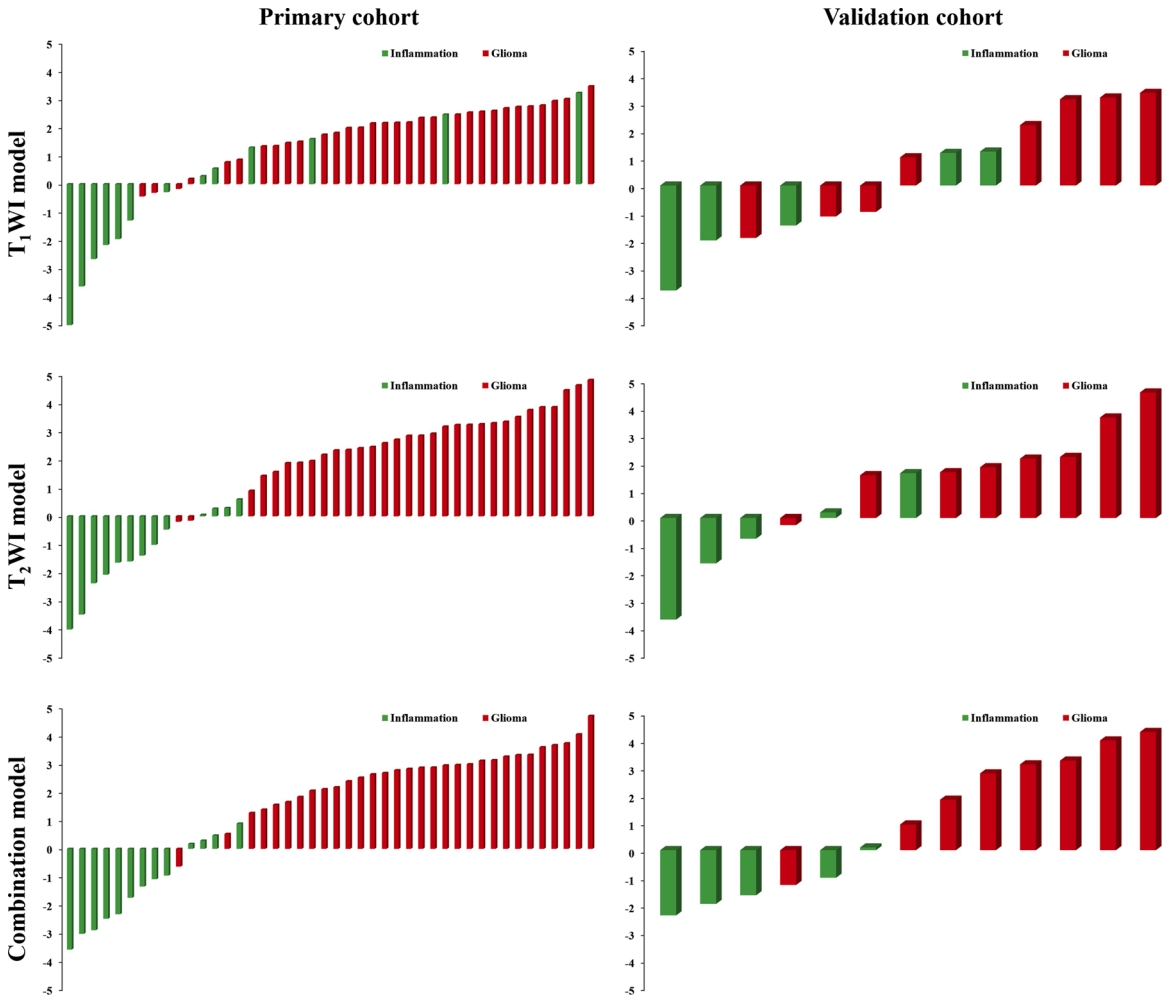

Fig. 4. Rad-score of different models for patients in primary and validation cohort.

have much more variable degrees of perinuclear cytoplasm and processes. Besides, the loss of alpha thalassemia retardation syndrome X-linked (ATRX), mutation of TP53 and isocitrate dehydrogenase (IDH) based on immunohistochemistry are detected in the glioma. In light of the 2016 World Health Organization (WHO) classification of central nervous system tumors, genetic changes such as status of 1p/19q deletion, mutation of IDH-1/2, and mutation of H3K27 M can provide more information on differential diagnosis. Consensus was achieved by discussion.

2.6. Radiologist's assessment

To compare the diagnostic performance of the radiomics signature with visual assessment, all 57 cases were independently reviewed by two associate professors of neuroradiology (G.b.C and Y.c.H with 27 and 17 years of neuroradiology experience, respectively). All patient names were de-identified prior to analysis and both radiologists had no prior knowledge of the final results. They had access to conventional MR images (T_1WI, T_2WI and T_1CE) and other functional sequences (depending on the MRI sequence requested by the clinician). In addition, clinical information (age, gender and onset) were also provided to the radiologists. Diagnosis was based on image and clinical analysis according to their respective clinical experience. They recorded the final diagnosis using a 4-point scale (1 = definite glioma; 2 = likely glioma; 3 = likely inflammation; and 4 = definite inflammation) [26]. To assess intra-observer agreement, radiologists re-evaluated images after a two months' washout period.

2.7. Statistical analysis

The normal distribution of data was investigated with Kolmogorov-Smirnov (K–S) test. Numerical variables with normal distribution were denoted as mean and standard deviation. Continuous and categorical variables were compared using two-sample *t*-test and Fisher's exact test, respectively. ICCs were used to assess intra- and inter-observer reproducibility of extracted features by two radiologists. Intra-observer agreements of radiologist's assessment were evaluated with Cohen's kappa coefficient. All statistical analyses above were performed with SPSS 20.0 software (IBM Corp, Chicago, IL, USA). Feature selection using two-sample *t*-test, Lasso regression algorithm, and correlation-matrix heat map generated using Pearson's correlation were carried out in R software (version 3.3.2). Receiver operating characteristic (ROC) curve analysis was performed to determine the performance of radiomics signature and radiologist's assessment, and accuracy and area under the curve (AUC) were obtained. Differences between the AUCs were compared by using a Delong test and performed using Medcalc version 18.5 software (MedCalc). $P < 0.05$ indicated a significant difference.

3. Results

3.1. Patients characteristics and feature robustness

Chronic inflammatory cell infiltration with reactive gliosis were found in 18 inflammations. All 39 grade II gliomas included 29 cases of

Table 3
Rad-score comparisons between inflammation and glioma in both the primary and validation cohort.

Model	Primary cohort			Validation cohort		
	Inflammation	Glioma	*P*	Inflammation	Glioma	*P*
T_1WI	−7.313 ± 2.793	1.890 ± 1.016	<0.001	−0.969 ± 2. 171	1.116 ± 2.175	0.120
T_2WI	−1.293 ± 1.451	2.697 ± 1.199	<0.001	−0.854 ± 2.000	2.178 ± 1.444	0.009
Combination	−1.349 ± 1.473	2.600 ± 1.066	<0.001	−1.373 ± 0.961	2.367 ± 1.828	0.002

P values were calculated by two-sample *t*-test.

Table 4
The diagnostic performance of three radiomics signature models.

Model	Primary cohort						Validation cohort					
	AUC	95 %CI	Sensitivity	Specificity	ACC	*P*	AUC	95 %CI	Sensitivity	Specificity	ACC	*P*
T_1WI	0.811	0.665−0.913	0.807	0.769	0.795	<0.001	0.775	0.505−1.000	0.500	1.000	0.615	0.107
T_2WI	0.980	0.947−1.000	0.936	1.000	0.955	<0.001	0.925	0.781−1.000	0.750	1.000	0.846	0.013
Combination	0.988	0.963−1.000	0.936	1.000	0.955	<0.001	0.950	0.833−1.000	0.875	1.000	0.923	0.008

P values were calculated by the receiver operating characteristic (ROC) curve analyses.
AUC = area under receiver-operating characteristic curve; CI = confidence interval; ACC = accuracy.

Table 5
The diagnostic performance of two radiologists.

Reader	AUC	95 %CI	ACC	ACC[§]	*P*
Radiologist A	0.661	0.519−0.802	0.719	0.544	0.047*
Radiologist B	0.722	0.591−0.854	0.737	0.526	0.005*

P values were calculated by the receiver operating characteristic (ROC) curve analyses. ACC = Number of cases with correct diagnosis (possible diagnosis (scale 2 and 3) + definite diagnosis (scale 1 and 4)) / 57; ACC[§] = Number of cases with definite diagnosis (scale 1 and 4) / 57.
AUC = area under receiver-operating characteristic curve; CI = confidence interval; ACC = accuracy.

diffuse astrocytoma, 6 cases of oligodendroglioma, and 4 cases of diffuse midline glioma. Relevant patient characteristics and MRI findings were summarized in Table 1. There were no significant differences in age, gender, onset and 2 MRI findings (side and ≥2 lobe involved) between the two groups ($P > 0.05$).

The ICCs of 45 features for both test-retest analysis (T_1WI, 0.816–1; T_2WI, 0.875–1) and interrater analysis (T_1WI, 0.756–1; T_2WI, 0.831–1) were greater than 0.75, thus were robust for further analysis (the segmentation results of the senior radiologist were used for further analysis).

3.2. Feature selection, radiomics signature score building and diagnostic validation

In the primary cohort, 19 features on T_1WI and 26 features on T_2WI with statistically significant difference between inflammation and glioma ($P < 0.05$) were selected using two sample *t*-test (Table 2). After the Lasso regression algorithm was applied for further feature reduction, 4 features in T_1WI model, 8 features in T_2WI model and 5 features in combination model (T_1WI + T_2WI) were chosen based on the corresponding lambda (λ) value with minimal deviance. The selected features and corresponding heat map of correlation matrix were shown in Fig. 3.

Three models of radiomics signature score were constructed with corresponding features selected above by means of linear combination according to their coefficients (**Supplementary material**). The rad-score for each patient in different modes are shown in waterfall plot (Fig. 4). In T_2WI and combination model, there was significant difference in rad-score between inflammation and glioma in both the primary and validation cohort (Table 3). In T_1WI model, the mean value of rad-score for patients with glioma was significantly higher than that of inflammation in primary cohort ($P < 0.001$), but no significant differences were found in validation cohort ($P = 0.120$).

The diagnostic performance of the three models was evaluated using the ROC curve of the primary and validation cohort (Table 4). In the primary cohort, T_2WI and combination models achieved higher diagnostic efficacy than T_1WI model with an AUC of 0.980 and 0.988, and the same accuracy of 0.955, for differentiating inflammation from glioma, respectively. In the validation cohort, efficacy of T_2WI and combination model was higher than T_1WI model for differentiating inflammation from glioma, with an AUC of 0.925 and 0.950, and the accuracy of 0.846 and 0.923, respectively.

Pairwise comparison of the AUCs revealed that significant differences were observed between T_2WI and T_1WI model ($P = 0.029$), and between combination and T_1WI model ($P = 0.013$) in both primary and validation cohort, but no significant differences were found between T_2WI and combination model ($P = 0.106$).

3.3. Radiologist's assessment

The diagnostic performance of the two radiologists were summarized in Table 5. AUC and accuracy of the more experienced radiologist B's assessment (AUC, 0.722; ACC, 0.737) were higher than those of radiologist A (AUC, 0.661; ACC, 0.719). Excluding the possible diagnosis (scale 2 and 3), the accuracy of only counting definite diagnosis (scale 1 and 4) is 0.544 for radiologist A, and 0.526 for radiologist B. However, no significant differences between AUCs from the two radiologists for differentiating inflammation from glioma ($P = 0.237$). Intra-observer agreement showed Kappa value of 0.813 for radiologist A and 0.865 for radiologist B.

4. Discussion

In atypical cases with no contrast enhancement, distinguishing inflammation from grade II glioma based on MRI is challenging. In the current study of 57 cases, T_1WI and T_2WI were adopted to investigate the diagnostic performance of radiomics features in discriminating inflammation from glioma. We found that the MR-based radiomics signature (T_2WI and combination model) was effective in discriminating inflammation from glioma, surpassing the level of experienced radiologist.

T_1WI and T_2WI (rather than advanced MRI sequences, which would prolong the scanning time and generate higher costs), are the most commonly used imaging sequence set in daily clinical practice for patients with suspected glioma [27]. In addition, the patient does not need to be injected with contrast medium during T_1WI and T_2WI scanning, which is beneficial to those with renal failure or contrast medium allergy

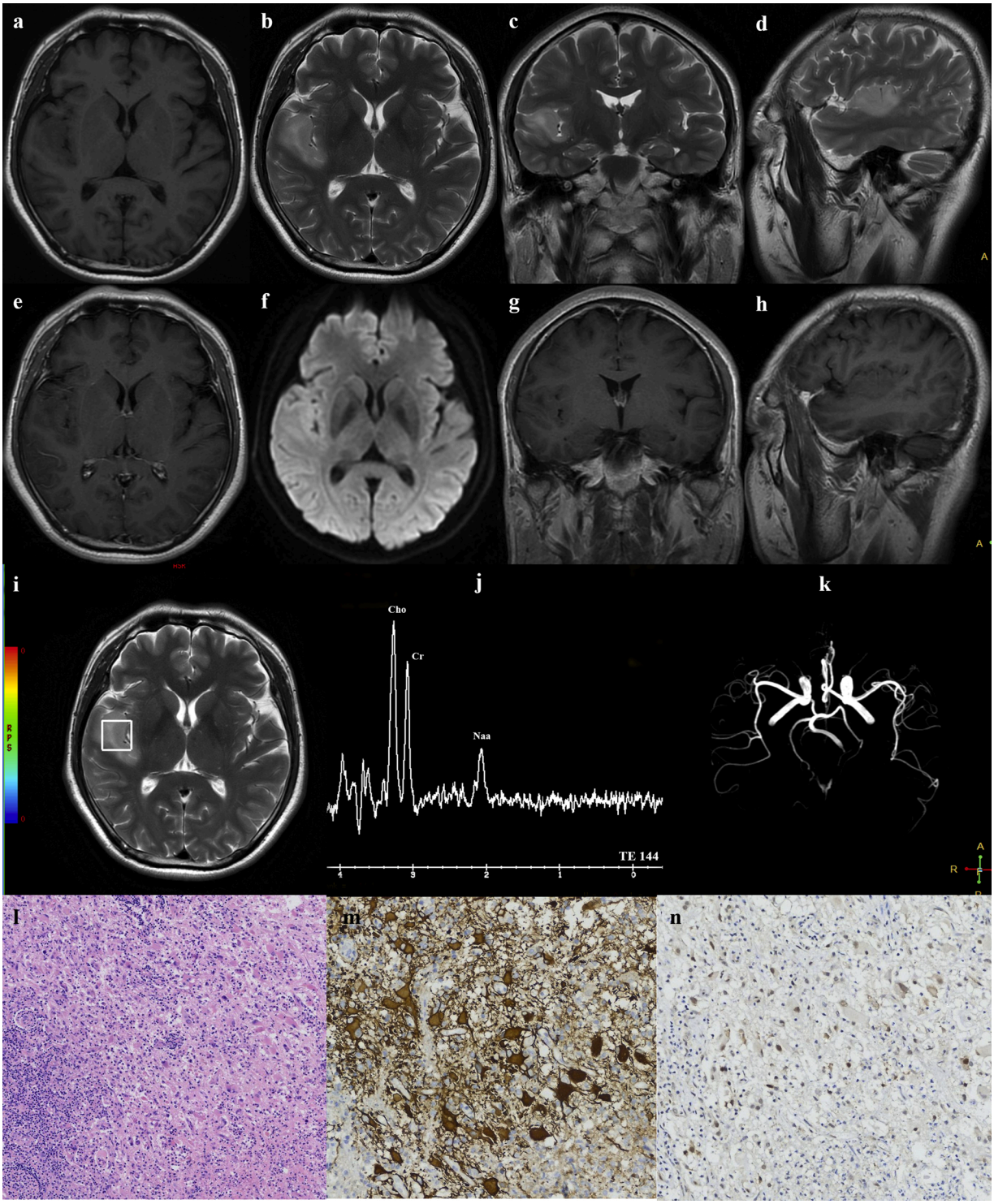

Fig. 5. A 45-year-old male presented with left limb weakness for 2 months. MRI showed right temporal lobe lesion with mass effect hypointense on T1WI (a), hyperintense on T_2WI (b, c, d), and no enhancement on T_1CE (e, g, h). Mild restricted diffusion was observed on DWI (f). The value of Cho/Naa on proton magnetic resonance spectroscopy (i, j) was 1.48. No abnormality was found on magnetic resonance angiography (k). Postoperative histopathology confirmed chronic inflammatory cell infiltration with reactive gliosis. (l), hematoxylin and eosin (H&E) staining (×100). (m), glial fibrillary acidic protein (GFAP) immunohistochemistry (×200). (n), alpha thalassemia retardation syndrome X-linked (ATRX) immunohistochemistry (×200). The case was misdiagnosed as glioma by two radiologists (radiologist A, scale 4; radiologist B, scale 3). Correct diagnosis was predicted by three radiomics signature models.

[28]. Therefore, using only two clinical routine sequences in the current study suggested that the proposed radiomics approach has the potential to be widely validated in clinical practice. To further investigate the contribution of each single MRI sequence for distinguishing inflammation from glioma, comparisons between T_1WI and T_2WI were performed. The diagnostic efficacy of T_2WI was better than that of T_1WI in primary and validation cohort. Moreover, 80 % of the features in the combination model are from T_2WI, indicating that T_2WI may provide more valuable information. Similar results were obtained in the study by Drabycz [29] and Petrujkić [30] where texture features extracted from

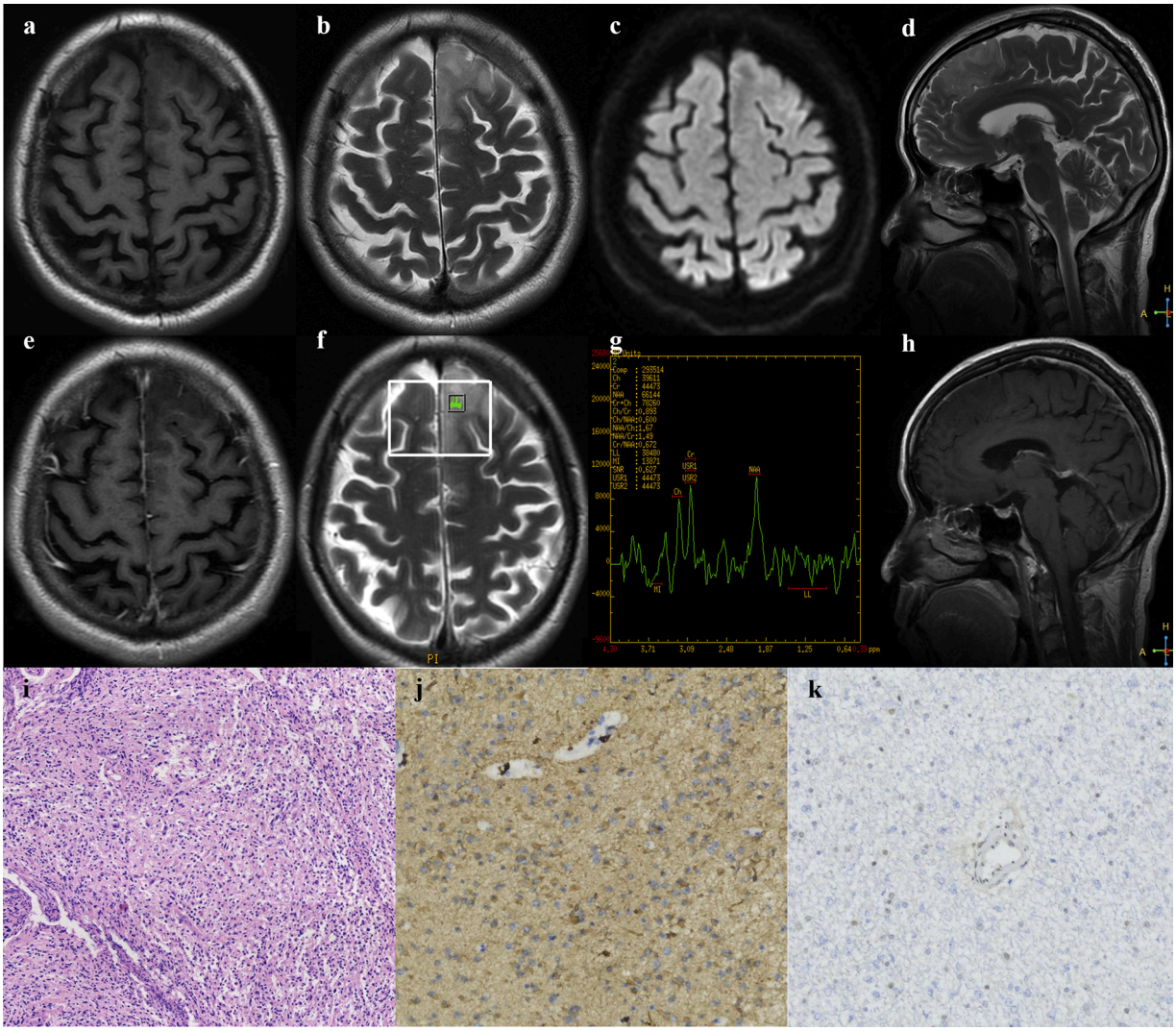

Fig. 6. A 64-year-old male presented with intermittent limb twitching with loss of consciousness for 4 months. MRI showed left frontal lobe lesion hypointense on T_1WI (a), hyperintense on T_2WI (b, d), and no enhancement on T_1CE (e, h). No restricted diffusion was observed on DWI (c). The value of Cho/Naa on proton magnetic resonance spectroscopy (f, g) was 0.60. Postoperative histopathology confirmed diffuse astrocytoma (World Health Organization grade II). (i), hematoxylin and eosin (H&E) staining (×100). (j), glial fibrillary acidic protein (GFAP) immunohistochemistry (×200). (k), alpha thalassemia retardation syndrome X-linked (ATRX) immunohistochemistry (×200). The case was misdiagnosed as inflammation by two radiologists (both rated as scale 1). Correct diagnosis was predicted by T_2WI and combination model, not T_1WI model.

T_2WI performs better in differential diagnostic tasks. The possible explanation might be the fact that ischemia, edema and glioma are considered more obvious on T_2WI, thus, texture features extracted from T_2WI potentially provided more information reflecting the pathophysiological changes of lesion than did on T_1WI. The much longer echo time on T_2WI may underlie this phenomenon [31]. However, interestingly, similar to previous study [32], combination model achieved higher AUC and ACC than did the use of either image model alone. The possible explanation is that biparametric MR images can provide more information than the single parameter image.

Redundant features are not conducive to model building. So Lasso is adopted in our study, a shrinkage method within linear regression models, which can automatically select features and produce sparse solutions [33]. It has the advantage of avoiding over fitting and is suitable for analyzing small samples with high-dimensional features. In our study, after the use of Lasso, fewer features are selected to reconstruct the radiomics signature (4 in T_1WI model, 8 in T_2WI model and 5 in combination model). It is worth noting that most of these selected features are first-order or second-order texture features, which have been proved to be very effective in distinguishing benign and malignant tumors [34–36].

The predictive performance based on radiomics signature was compared with radiologist's assessment for the first time. Although the diagnosis of senior radiologists was based on more abundant clinical and imaging information (including medical history, laboratory tests, enhanced MR sequences and some functional MR sequences), the accuracy of radiologist was lower than that of the radiomics signature. Notably, the diagnostic accuracy of radiologists based on definitive diagnoses (score 1 and 4) was 0.544 for radiologist A and 0.526 for radiologist B, respectively. The inconsistency between rich information and low diagnostic efficacy can be explained with three possible reasons. First, similar clinical manifestations and atypical laboratory tests in misdiagnosed cases make differential diagnosis difficult. As reported in the literature, despite of advanced molecular and serological diagnostic techniques, the causative pathogen of encephalitis cannot be detected in up to 60 % cases [37]. Second, unlike previous studies [11–14], which focus on high-grade gliomas, enhancement pattern plays an important role in differential diagnosis. However, all of our subjects were no contrast enhancement on post-contrast T_1WI. Furthermore, the functional MR (as shown in Figs. 5 and 6) features overlap between

inflammation and glioma, making differential diagnosis difficult. Finally, interpretation of image feature is subjective, leading to potential bias. Moreover, even for senior radiologists, the subtle image feature differences are difficult to be recognized by visualization, and radiomics signature based on quantitative parameters can better characterize the lesion and further improve the discrimination of these two conditions.

Although our study showed the potential usefulness of the radiomics signature in differentiating inflammation from glioma, there are several limitations. First, the sample size of retrospective study was relatively small, mainly because of the low clinical incidence of atypical cases, especially in the inflammation group. Second, the primary and validation cohorts were performed on the same MRI scanner. The robustness of our results remains to be validated with different scanners from multiple centers in the future. Third, the diagnosis of inflammation was based on postoperative histopathology, but its etiology was unknown.

In conclusion, our results demonstrate the potential use of radiomics signature based on conventional MR sequences in differentiating inflammation from grade II gliomas in non-contrast enhanced populations. Compared to the experience-dependent visual-based conventional reading strategy, radiomics signature exhibited better diagnostic performances, which indicates its potential application in assisting the clinical decision making.

Funding

This study received financial support from the National Key Research and Development Program of China (No.2016YFC0107105, Dr. Cui GB), Young Talent Foundation of Tangdu Hospital (Dr. Wang W) and Key Industrial Chain Projects in the Field of Social Development of Shaanxi Province (No. 2019ZDLSF02-07, Dr. Cui GB), Hovering Program of Fourth Military Medical University (axjhww, to WW) and the Talent Foundation of Tangdu Hospital (2018BJ003 to WW).

CRediT authorship contribution statement

Yu Han: Conceptualization, Writing - original draft, Formal analysis. **Yang Yang:** Methodology, Software, Data curation. **Zhe-sheng Shi:** Visualization, Investigation. **An-ding Zhang:** Software, Investigation. **Lin-feng Yan:** . **Yu-chuan Hu:** Validation, Investigation. **Lan-lan Feng:** Resources, Data curation. **Jiao Ma:** Resources, Validation. **Wen Wang:** Funding acquisition, Writing - review & editing. **Guang-bin Cui:** Supervision, Funding acquisition, Writing - review & editing.

Declaration of Competing Interest

The authors declare no conflict of interest.

Acknowledgments

We would like to thank Dr. Xiao-Cheng Wei from GE healthcare for providing technical support.

Appendix A. Supplementary data

Supplementary material related to this article can be found, in the online version, at doi:https://doi.org/10.1016/j.ejrad.2020.109467.

References

[1] S. Lapointe, A. Perry, N.A. Butowski, Primary brain tumours in adults, Lancet 392 (10145) (2018) 432–446, https://doi.org/10.1016/S0140-6736(18)30990-5.
[2] M.M. Thurnher, P.C. Sundgren, Intracranial infection and inflammation, in: J. Hodler, R.A. Kubik-Huch, G.K. von Schulthess (Eds.), Diseases of the Brain, Head and Neck, Spine 2020-2023: Diagnostic Imaging, 2020, pp. 59–76. Cham (CH).
[3] S. Talathi, N. Gupta, N. Reddivalla, S. Prokhorov, M. Gold, Anaplastic astrocytoma mimicking herpes simplex encephalitis in 13-year old girl, Eur. J. Paediatr. Neurol. 19 (6) (2015) 722–725, https://doi.org/10.1016/j.ejpn.2015.07.007.
[4] R. Nagata, K. Ikeda, Y. Nakamura, Y. Ishikawa, K. Miura, R. Sato, Y. Kawase, K. Kawabe, Y. Iwasaki, A case of gliomatosis cerebri mimicking limbic encephalitis: malignant transformation to glioblastoma, Intern. Med. 49 (13) (2010) 1307–1310, https://doi.org/10.2169/internalmedicine.49.3278.
[5] K. Piper, H. Foster, B. Gabel, B. Nabors, C. Cobbs, Glioblastoma mimicking viral encephalitis responds to acyclovir: a case series and literature review, Front. Oncol. 9 (2019) 8, https://doi.org/10.3389/fonc.2019.00008.
[6] J. Lu, J.H. Zhang, A.L. Miao, J.X. Yin, D.L. Zhu, X.J. Lin, D.W. Chen, J.P. Shi, Brain astrocytoma misdiagnosed as anti-NMDAR encephalitis: a case report, BMC Neurol. 19 (1) (2019) 210, https://doi.org/10.1186/s12883-019-1436-x.
[7] D. Panagopoulos, M. Themistocleous, K. Apostolopoulou, G. Sfakianos, Herpes simplex encephalitis initially erroneously diagnosed as glioma of the cerebellum: case report and literature review, World Neurosurg. 129 (2019) 421–427, https://doi.org/10.1016/j.wneu.2019.06.158.
[8] A. Vogrig, B. Joubert, F. Ducray, L. Thomas, C. Izquierdo, K. Decaestecker, O. Martinaud, E. Gerardin, S. Grand, J. Honnorat, Glioblastoma as differential diagnosis of autoimmune encephalitis, J. Neurol. 265 (3) (2018) 669–677, https://doi.org/10.1007/s00415-018-8767-1.
[9] A.M. Blamire, MR approaches in neurodegenerative disorders, Prog. Nucl. Magn. Reson Spectrosc. 108 (2018) 1–16, https://doi.org/10.1016/j.pnmrs.2018.11.001.
[10] J.G. Smirniotopoulos, H.R. Jager, Differential diagnosis of intracranial masses, in: J. Hodler, R.A. Kubik-Huch, G.K. von Schulthess (Eds.), Diseases of the Brain, Head and Neck, Spine 2020-2023: Diagnostic Imaging, 2020, pp. 93–104. Cham (CH).
[11] M. Zoccarato, S. Valeggia, L. Zuliani, M. Gastaldi, S. Mariotto, D. Franciotta, S. Ferrari, G. Lombardi, V. Zagonel, P. De Gaspari, M. Ermani, A. Signori, A. Pichiecchio, B. Giometto, R. Manara, Conventional brain MRI features distinguishing limbic encephalitis from mesial temporal glioma, Neuroradiology 61 (8) (2019) 853–860, https://doi.org/10.1007/s00234-019-02212-1.
[12] S.B. Hiremath, A. Muraleedharan, S. Kumar, C. Nagesh, C. Kesavadas, M. Abraham, T.R. Kapilamoorthy, B. Thomas, Combining diffusion tensor metrics and dsc perfusion imaging: can it improve the diagnostic accuracy in differentiating tumefactive demyelination from high-grade glioma? AJNR Am. J. Neuroradiol. 38 (4) (2017) 685–690, https://doi.org/10.3174/ajnr.A5089.
[13] C.H. Toh, K.C. Wei, S.H. Ng, Y.L. Wan, M. Castillo, C.P. Lin, Differentiation of tumefactive demyelinating lesions from high-grade gliomas with the use of diffusion tensor imaging, AJNR Am. J. Neuroradiol. 33 (5) (2012) 846–851, https://doi.org/10.3174/ajnr.A2871.
[14] M.C. Mabray, B.A. Cohen, J.E. Villanueva-Meyer, F.E. Valles, R.F. Barajas, J. L. Rubenstein, S. Cha, Performance of apparent diffusion coefficient values and conventional mri features in differentiating tumefactive demyelinating lesions from primary brain neoplasms, AJR Am. J. Roentgenol. 205 (5) (2015) 1075–1085, https://doi.org/10.2214/AJR.14.13970.
[15] P. Lambin, R.T.H. Leijenaar, T.M. Deist, J. Peerlings, E.E.C. de Jong, J. van Timmeren, S. Sanduleanu, R. Larue, A.J.G. Even, A. Jochems, Y. van Wijk, H. Woodruff, J. van Soest, T. Lustberg, E. Roelofs, W. van Elmpt, A. Dekker, F. M. Mottaghy, J.E. Wildberger, S. Walsh, Radiomics: the bridge between medical imaging and personalized medicine, Nat. Rev. Clin. Oncol. 14 (12) (2017) 749–762, https://doi.org/10.1038/nrclinonc.2017.141.
[16] W.L. Bi, A. Hosny, M.B. Schabath, M.L. Giger, N.J. Birkbak, A. Mehrtash, T. Allison, O. Arnaout, C. Abbosh, I.F. Dunn, R.H. Mak, R.M. Tamimi, C.M. Tempany, C. Swanton, U. Hoffmann, L.H. Schwartz, R.J. Gillies, R.Y. Huang, H. Aerts, Artificial intelligence in cancer imaging: clinical challenges and applications, CA Cancer J. Clin. 69 (2) (2019) 127–157, https://doi.org/10.3322/caac.21552.
[17] E. Sala, E. Mema, Y. Himoto, H. Veeraraghavan, J.D. Brenton, A. Snyder, B. Weigelt, H.A. Vargas, Unravelling tumour heterogeneity using next-generation imaging: radiomics, radiogenomics, and habitat imaging, Clin. Radiol. 72 (1) (2017) 3–10, https://doi.org/10.1016/j.crad.2016.09.013.
[18] J.Y. Kim, J.E. Park, Y. Jo, W.H. Shim, S.J. Nam, J.H. Kim, R.E. Yoo, S.H. Choi, H. S. Kim, Incorporating diffusion- and perfusion-weighted MRI into a radiomics model improves diagnostic performance for pseudoprogression in glioblastoma patients, Neuro Oncol 21 (3) (2019) 404–414, https://doi.org/10.1093/neuonc/noy133.
[19] R. Jain, L.M. Poisson, D. Gutman, L. Scarpace, S.N. Hwang, C.A. Holder, M. Wintermark, A. Rao, R.R. Colen, J. Kirby, J. Freymann, C.C. Jaffe, T. Mikkelsen, A. Flanders, Outcome prediction in patients with glioblastoma by using imaging, clinical, and genomic biomarkers: focus on the nonenhancing component of the tumor, Radiology 272 (2) (2014) 484–493, https://doi.org/10.1148/radiol.14131691.
[20] B. Kocak, E.S. Durmaz, P. Kadioglu, O. Polat Korkmaz, N. Comunoglu, N. Tanriover, N. Kocer, C. Islak, O. Kizilkilic, Predicting response to somatostatin analogues in acromegaly: machine learning-based high-dimensional quantitative texture analysis on T2-weighted MRI, Eur. Radiol. 29 (6) (2019) 2731–2739, https://doi.org/10.1007/s00330-018-5876-2.
[21] B. Zhang, K. Chang, S. Ramkissoon, S. Tanguturi, W.L. Bi, D.A. Reardon, K.L. Ligon, B.M. Alexander, P.Y. Wen, R.Y. Huang, Multimodal MRI features predict isocitrate dehydrogenase genotype in high-grade gliomas, Neuro Oncol 19 (1) (2017) 109–117, https://doi.org/10.1093/neuonc/now121.
[22] J. Yu, Z. Shi, Y. Lian, Z. Li, T. Liu, Y. Gao, Y. Wang, L. Chen, Y. Mao, Noninvasive IDH1 mutation estimation based on a quantitative radiomics approach for grade II glioma, Eur. Radiol. 27 (8) (2017) 3509–3522, https://doi.org/10.1007/s00330-016-4653-3.
[23] M.M. Galloway, Texture analysis using gray level run lengths, 4(2) 172-179.
[24] S. Wu, J. Zheng, Y. Li, H. Yu, S. Shi, W. Xie, H. Liu, Y. Su, J. Huang, T. Lin, A radiomics nomogram for the preoperative prediction of lymph node metastasis in bladder cancer, Clin. Cancer Res. 23 (22) (2017) 6904–6911, https://doi.org/10.1158/1078-0432.CCR-17-1510.

[25] R. Tibshirani, Regression Shrinkage and Selection Via the Lasso, Journal of the Royal Statistical Society 58(1) 267-288.
[26] H.B. Suh, Y.S. Choi, S. Bae, S.S. Ahn, J.H. Chang, S.G. Kang, E.H. Kim, S.H. Kim, S. K. Lee, Primary central nervous system lymphoma and atypical glioblastoma: differentiation using radiomics approach, Eur. Radiol. 28 (9) (2018) 3832–3839, https://doi.org/10.1007/s00330-018-5368-4.
[27] C.F. Freyschlag, S.M. Krieg, J. Kerschbaumer, D. Pinggera, M.T. Forster, D. Cordier, M. Rossi, G. Miceli, A. Roux, A. Reyes, S. Sarubbo, A. Smits, J. Sierpowska, P. A. Robe, G.J. Rutten, T. Santarius, T. Matys, M. Zanello, F. Almairac, L. Mondot, A. S. Jakola, M. Zetterling, A. Rofes, G. von Campe, R. Guillevin, D. Bagatto, V. Lubrano, M. Rapp, J. Goodden, P.C. De Witt Hamer, J. Pallud, L. Bello, C. Thome, H. Duffau, E. Mandonnet, Imaging practice in low-grade gliomas among European specialized centers and proposal for a minimum core of imaging, J. Neurooncol. 139 (3) (2018) 699–711, https://doi.org/10.1007/s11060-018-2916-3.
[28] F. National Kidney, K/DOQI clinical practice guidelines for chronic kidney disease: evaluation, classification, and stratification, Am. J. Kidney Dis. 39 (2 Suppl 1) (2002) S1–266.
[29] S. Drabycz, G. Roldan, P. de Robles, D. Adler, J.B. McIntyre, A.M. Magliocco, J. G. Cairncross, J.R. Mitchell, An analysis of image texture, tumor location, and MGMT promoter methylation in glioblastoma using magnetic resonance imaging, Neuroimage 49 (2) (2010) 1398–1405, https://doi.org/10.1016/j.neuroimage.2009.09.049.
[30] K. Petrujkic, N. Milosevic, N. Rajkovic, D. Stanisavljevic, S. Gavrilovic, D. Dzelebdzic, R. Ilic, A. Di Ieva, R. Maksimovic, Computational quantitative MR image features - a potential useful tool in differentiating glioblastoma from solitary brain metastasis, Eur. J. Radiol. 119 (2019) 108634, https://doi.org/10.1016/j.ejrad.2019.08.003.
[31] X. Chen, X. Wei, Z. Zhang, R. Yang, Y. Zhu, X. Jiang, Differentiation of true-progression from pseudoprogression in glioblastoma treated with radiation therapy and concomitant temozolomide by GLCM texture analysis of conventional MRI, Clin. Imaging 39 (5) (2015) 775–780, https://doi.org/10.1016/j.clinimag.2015.04.003.
[32] Y. Han, L.F. Yan, X.B. Wang, Y.Z. Sun, X. Zhang, Z.C. Liu, H.Y. Nan, Y.C. Hu, Y. Yang, J. Zhang, Y. Yu, Q. Sun, Q. Tian, B. Hu, G. Xiao, W. Wang, G.B. Cui, Structural and advanced imaging in predicting MGMT promoter methylation of primary glioblastoma: a region of interest based analysis, BMC Cancer 18 (1) (2018) 215, https://doi.org/10.1186/s12885-018-4114-2.
[33] S. Mueller-Using, T. Feldt, F.S. Sarfo, K.A. Eberhardt, Factors associated with performing tuberculosis screening of HIV-positive patients in Ghana: LASSO-based predictor selection in a large public health data set, BMC Public Health 16 (2016) 563, https://doi.org/10.1186/s12889-016-3239-y.
[34] Y. She, L. Zhang, H. Zhu, C. Dai, D. Xie, H. Xie, W. Zhang, L. Zhao, L. Zou, K. Fei, X. Sun, C. Chen, The predictive value of CT-based radiomics in differentiating indolent from invasive lung adenocarcinoma in patients with pulmonary nodules, Eur. Radiol. 28 (12) (2018) 5121–5128, https://doi.org/10.1007/s00330-018-5509-9.
[35] J. Guo, Z. Liu, C. Shen, Z. Li, F. Yan, J. Tian, J. Xian, MR-based radiomics signature in differentiating ocular adnexal lymphoma from idiopathic orbital inflammation, Eur. Radiol. 28 (9) (2018) 3872–3881, https://doi.org/10.1007/s00330-018-5381-7.
[36] G. Xiao, W.C. Rong, Y.C. Hu, Z.Q. Shi, Y. Yang, J.L. Ren, G.B. Cui, MRI radiomics analysis for predicting the pathologic classification and tnm staging of thymic epithelial tumors: a pilot study, AJR Am. J. Roentgenol. 214 (2) (2020) 328–340, https://doi.org/10.2214/AJR.19.21696.
[37] P.G.E. Kennedy, P.L. Quan, W.I. Lipkin, Viral encephalitis of unknown cause: current perspective and recent advances, Viruses 9 (6) (2017), https://doi.org/10.3390/v9060.